Nuclear Science and Techniques (2026) 37:91
https://doi.org/10.1007/s41365-026-01916-3

# Comparative evaluation of single-mask and single-shot X-ray phase-contrast and dual-energy computed tomography analyses on soft-tissue phantom

Chang Li[1,2] · Xiao-Xuan Ren[1,2] · Liang-Liang Lv[1,2,3] · Shu-Yi Sun[1,2] · Jian Zhang[1,2] · Yin-Qi Lei[1,2] · Xiao-Dong Pan[1,2] · Cui Zhang[3] · Gong-Ping Li[1,2,4]

Received: 4 August 2024 / Revised: 12 November 2024 / Accepted: 22 November 2024 / Published online: 10 March 2026


## Abstract

In clinical diagnosis, conventional X-ray absorption-contrast computed tomography (XACT) technology cannot effectively differentiate diseased tissues from the healthy ones. X-ray phase-contrast CT (XPCT) and dual-energy CT (DECT), emerging X-ray imaging technologies with superior diagnostic capabilities, address this issue through different principles. While both XPCT and DECT have advantages and disadvantages in medical applications, their systematic comparison is lacking. Using GEANT4 and MATLAB, in this study, we established an X-ray phase-contrast imaging (XPCI) model based on single-mask and single-shot edge illumination for fast XPCT imaging, comparing it with DECT on soft-tissue phantom. XACT served as a reference for comparison. The study introduces an evaluation system using statistical measures including absolute error, mean absolute error, structure similarity index measure, peak signal-to-noise ratio, and contrast-to-noise ratio. Results show XPCT images are superior to DECT. The XPCI model can be improved on existing medical CT for widespread medical application.

**Keywords** Comparative evaluation · X-ray phase-contrast CT · Edge illumination · Dual-energy CT · GEANT4

## 1 Introduction

X-ray imaging is ubiquitous in clinical diagnosis and has common applications in digital radiography (DR) and computed tomography (CT). DR provides two-dimensional absorption imaging, whereas CT offers slices and three-dimensional absorption imaging. Compared with DR, CT effectively addresses the issue of overlapping projection information. Despite this, current X-ray absorption-contrast CT (XACT) performs exceptionally well for imaging highly absorbing objects but still faces challenges in the imaging of weakly absorbing objects or those with similar absorption characteristics [1, 2], potentially leading to patients missing the optimal treatment period. To overcome the limitations of XACT, dual-energy CT (DECT) and X-ray phase-contrast CT (XPCT) have been proposed to address the issue [3–5]. The former utilizes two different X-ray energy spectra to distinguish materials, whereas the latter combines X-ray phase-contrast imaging (XPCI) and CT to extract the phase information of materials. The popular XPCI methods include crystal interference (CI) [6], propagation-based imaging (PBI) [7–9], speckle imaging [10, 11],

This work was supported by the National Natural Science Foundation of China (No. 12105267), National Natural Science Foundation of China (No. 11975006), Major Special Program of Science and Technology of Gansu Province (No. 1ZD8JA002), the Fundamental Research Funds for the Central Universities (No. lzujbky-2020-pd02), and the China Postdoctoral Science Foundation (No. 2019M653792).

✉ Cui Zhang
zhangcui@caep.cn

✉ Gong-Ping Li
ligp@lzu.edu.cn

1 Frontiers Science Center for Rare Isotopes, Lanzhou University, Lanzhou 730000, China

2 School of Nuclear Science and Technology, Lanzhou University, Lanzhou 730000, China

3 Institute of Chemical Materials, China Academy of Engineering Physics, Mianyang 621000, China

4 Key Laboratory of Special Function Materials and Structure Design, Ministry of Education, Lanzhou University, Lanzhou 730000, China

analyzer-based imaging (ABI) [12–14], grating interference (GI) [15–20], and edge illumination (EI) [21–23]. ABI, GI, and EI can measure phase signals using conventional X-ray sources. However, ABI and GI face challenges due to low usable flux and high system stability requirements. EI offers advantages through lower coherence and alignment needs, and better stability. Compared to DECT, XPCT extracts more significant phase information and remains an emerging imaging technology. However, XPCT needs additional optical components to convert phase information into measurable intensity signals, requiring complex equipment, stringent optical components, and optimized system design. For details on XPCI methods' benefits and challenges, see reference [1]. Therefore, addressing these challenges is critical for the development of XPCT.

However, while DECT has gradually become more popular and has been applied in clinical diagnosis because of its excellent ability to identify components, the application of XPCT technology in medicine remains at the research stage because of the complexity of the device, which lags behind that of DECT in terms of medical implementation. Given the widespread use of DECT, the feasibility and necessity of XPCT in the medical field must be reconsidered. Both XPCT and DECT have advantages and disadvantages in medical applications. However, a systematic comparison of these two technologies is currently lacking. To compare the performance of XPCT in medical imaging with that of DECT, Zhang et al. [4] evaluated and compared the two techniques using the CHO model and theoretically analyzing the preferred order of application for XPCT and DECT in different CT spatial resolution scenarios. They employed the GI method in XPCT and noted that the XPCT relies on the spatial resolution of images and is more suitable for ultrahigh spatial resolution imaging tasks of small objects. In their distinguished work, some limitations of GI-based XPCT imaging were observed. The size of the grating and detector devices limited the size of the imaged object. Furthermore, their work based on a numerical simulation was significantly different from the actual results, and the Monte Carlo-based simulation we used was closer to reality. Additionally, the precision of the displacement system is more challenging for actual GI scanning and data acquisition, particularly for imaging methods that use interference [24, 25]. This is also a challenge in current medical applications of XPCT technology, which utilizes the temporal coherence of radiation. In addition to the GI method, the EI method holds promise for the widespread application of XPCT technology. The EI-based XPCT method is a non-interference imaging technique with a simpler mask and detector configuration than GI, facilitating easier imaging of large objects [26]. Furthermore, the EI-based XPCT method can be simulated using GEANT4, a feat challenging to accomplish using interferometric methods. The results of the EI-based XPCT simulations in this study are different from theirs because of differences in the XPCT method and simulation tools. In addition, a more comprehensive and specific statistical evaluation is required to compare the advantages and disadvantages of DECT and EI-based XPCT imaging, which will be discussed in detail later.

XPCT is currently undergoing rapid development; however, matching the device simplicity of XACT or DECT remains challenging. Single-mask and single-shot (SMSS) EI stands out among XPCTs, adding an optical component to existing clinical CT devices to extract phase information efficiently.

Classical EI imaging uses two absorption masks—one before the object and one before the detector, requiring multiple exposures through mask displacement. Although displacement requirements are less stringent than GI, the double mask makes imaging cumbersome. This paper uses SMSS EI model [27], retaining only the object mask and using adjacent pixel pairs as detection units for single-exposure imaging. Considering practical applications, sacrificing some resolution for a simpler SMSS method is optimal. SMSS EI-based XPCT can be improved on existing medical CT equipment.

In this study, we built a complete set of SMSS EI imaging models and algorithms based on GEANT4 and MATLAB for quantitative evaluation using XACT and DECT at the same dose. To demonstrate the differences among the three techniques more intuitively, we directly used the physical quantities reconstructed using MATLAB as the reconstructed image contrast for evaluation. To assess the image quality of the three techniques, a statistical evaluation system was implemented, including absolute error (AE), mean absolute error (MAE), structure similarity index measure (SSIM), peak signal-to-noise ratio (PSNR), and contrast-to-noise ratio (CNR). Through this work, we not only quantitatively compared the differences between XACT, DECT, and XPCT, confirming the superiority of XPCT, but also provided an alternative and fast solution for XPCT medical applications.

## 2 Methods and materials

### 2.1 Imaging technologies

In theory, as X-rays pass through an object, not only do their intensity attenuate, but their phase also shifts. This can be explained well by the refractive index formula $n = 1 - \delta + i\beta$, where $\beta$ represents the absorption factor and $\delta$ represents the phase-shift factor. Both XACT and DECT extract the intensity attenuation of X-rays, whereas XPCT focuses on extracting the phase-shift of the X-rays. Considering that the emission energy spectrum of the X-ray is $\Omega(E)$ and the spatial position of the

object under test is $(x, y, z)$, where the direction of $\vec{z}$ is from the source to the center of the detector, the absorption projection quantity $P(s, \theta)$ of the detector in different directions $\theta$ can be expressed as follows:

$$P(s,\theta) = \int_{\Omega}\int_{l_{\text{front}}}^{l_{\text{end}}} \mu(x,y,z)\cdot Dirac(s - x\cos\theta - y\sin\theta)\,\mathrm{d}l\mathrm{d}E \tag{1}$$

where *Dirac* represents the Dirac function, $s$ represents the projection distance, $l$ is the propagation distance of the X-rays within the object, $l_{\text{front}}$ indicates the position at which the X-rays enter the object, and $l_{\text{end}}$ represents the position at which the X-rays exit the object. Equation 1 is a modified form of the Lambert–Beer law. By collecting multiple projections at different angles and subsequently employing filtered back-projection (FBP) reconstruction algorithms, the distribution of absorption coefficients within an object can be calculated and reconstructed, yielding either slice or three-dimensional images.

DECT employs a widely used basis material decomposition model leveraging the distinct absorption coefficient $\mu$ characteristics of objects under varying X-ray energies. Through mathematical modeling, the imaging data were decomposed on different bases. In this process, the linear attenuation coefficient $\mu(x, y, z)$ is transformed into $\mu_{\text{L}}(x, y, z) + \mu_{\text{H}}(x, y, z)$, where the subscripts L and H represent the conditions of low and high X-ray tube voltages, respectively. Correspondingly, the projection quantity $P$ that describes DECT-based absorption projection formula is transformed as follows:

$$\begin{aligned} P_{\text{L/H}}(s,\theta) = \ln\int \Omega_{\text{L/H}}\,\mathrm{d}E - \ln\int_{\Omega_{\text{L/H}}}\int_{l_{\text{front}}}^{l_{\text{end}}} \Omega_{\text{L/H}} \\ \cdot\exp\left[-b_1\cdot\mu_{\text{L/H}}(x,y,z)\cdot Dirac(s - x\cos\theta - y\sin\theta)\right. \\ \left. -b_2\cdot\mu_{\text{L/H}}(x,y,z)\cdot Dirac(s - x\cos\theta - y\sin\theta)\right]\mathrm{d}l\mathrm{d}E \end{aligned} \tag{2}$$

where $b_1$ and $b_2$ represent decomposition coefficients. Given the projection data from the dual-energy spectra, $b_1$ and $b_2$ can be obtained by solving the system in Eq. 2. Using calcium and water as the basis for decomposition, the relative electron density $\rho_{\text{e}}$ and effective atomic number $Z_{\text{eff}}$ of the object can be represented by Eqs. 3 and 4.

$$\rho_{\text{e}} = b_1\cdot\rho_{\text{e,calcium}} + b_2\cdot\rho_{\text{e,water}} \tag{3}$$

$$\begin{aligned} Z_{\text{eff}} &= \left(\frac{b_1\cdot\rho_{\text{e,calcium}}Z_{\text{calcium}}^{n} + b_2\cdot\rho_{\text{e,water}}Z_{\text{water}}^{n}}{b_1\cdot\rho_{\text{e,calcium}} + b_2\cdot\rho_{\text{e,water}}}\right)^{1/n}, \\ n &= 4\sim 5 \end{aligned} \tag{4}$$

where $\rho_{\text{e,calcium}}$ and $\rho_{\text{e,water}}$ are the electron densities of calcium and water, respectively; and $Z_{\text{calcium}}$ and $Z_{\text{water}}$ are the effective atomic numbers of calcium and water, respectively. Equations 3 and 4 reflect the absorption contrast of the material at different energies.

Unlike the first two techniques, XPCT extracts phase-shift information from X-rays. The double-mask EI method requires the illumination curve (IC) to be read by moving the two masks laterally relative to each other. IC acquisition required at least three exposures. Absorption, refraction, and scattering information can be obtained in the presence and absence of an object, which means that the imaging process requires the positional alignment of the two optics and multiple exposures, and the accuracy and stability requirements of the system are challenging for clinical conditions. The SMSS EI method utilizes two adjacent pixels to detect the offset of beamlets in a single exposure, thereby quantitatively extracting refraction information, as shown in Eq. 5 [28].

$$\triangle\theta_y = \frac{W}{2Z_{\text{od}}}\frac{I_1 - I_2}{I_1 + I_2} \tag{5}$$

where $W$ is the distribution of individual beamlets on the detector related to the experimental conditions, $Z_{\text{od}}$ is the distance from the object to the detector, and $I_1$ and $I_2$ are the intensity values of two neighboring pixels. SMSS EI achieves concise and efficient single-exposure imaging with a certain loss of spatial resolution, which is significantly less difficult to implement and reduces the time and dose required for imaging. This loss of resolution can be compensated for by two dither steps, which are equivalent to a two-exposure imaging method. The quantum projection quantity of the differential phase is expressed as

$$\triangle\theta_y = k\int_{l_{\text{front}}}^{l_{\text{end}}}\frac{\partial\delta(x,y,z)}{\partial y}\,\mathrm{d}l, \tag{6}$$

where $k$ represents a constant that enables the reconstruction of phase information $\delta$. However, the term $\partial\delta/\partial y$ is a vector that cannot be used directly in conventional FBP algorithms. This issue was encountered in the earliest attempts at ABI to reconstruct phase information. Zhu et al. [29, 30] multiplied the term by $\cos\theta$ for each projection, thus transforming the $\partial\delta/\partial y\cdot\cos\theta$ term into an invariant. In addition to the indirect method, the direct integration of $\partial\delta/\partial y$ to obtain $\delta$ is another reconstruction method. Another direct method uses a Hilbert filter to directly resolve the $\delta$ signal using $\partial\delta/\partial y$. A more detailed reconstruction algorithm for the phase information can be found in Zhang's paper [31].

## 2.2 Simulation model

We used GEANT4 version 11.1.0, with Ubuntu 20.04.02, for all the simulations. The GEANT4 simulations were run on a desktop machine with an Intel Core i7-13700KF 5.40 GHz CPU processor. The simulations involve the physical principles of electromagnetism and X-ray refraction,

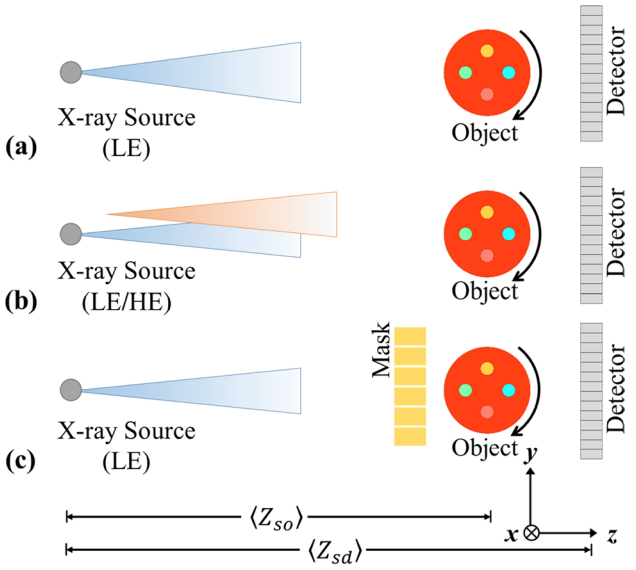


**Fig. 1** (Color online) Schematics of the three systems. **a** depicts XACT system, **b** depicts DECT system, and **c** depicts SMSS EI-based XPCT system

adhering to the Beer–Lambert law (considering photon-matter interactions such as the photoelectric effect and Compton effect, but excluding electron pair effects as photon energies are below 1.02 MeV in our setup) and Snell's law (refracting X-rays when transitioning between media based on their refractive indexes). *G4ElectromagneticPhysics* is used to make X-ray follow the absorption process, and *G4MaterialPropertiesTable* is used to define the *RINDEX* of an object to make X-ray follow the refraction process. The emitted particles employ the *G4GeneralParticleSource* module using the command */gps/hist/point* to weigh the energy of each emitted photon based on the corresponding energy spectrum intensity.

The GEANT4 configurations of the three systems are presented in Fig. 1. $Z_{so}$ is the distance from the source to the object and $Z_{sd}$ is the distance from the source to the detector, with values of 80 and 100 cm, respectively. The XACT system is a basic device consisting of an X-ray source, an object, and a detector, where the energy of the X-ray source corresponds only to the low-energy option. The DECT system adds a high-energy X-ray source to the XACT system. The XPCT system utilizes the SMSS EI method by adding a coded-aperture module to the XACT system as a mask.

The specific parameters for CT imaging are listed in Table 1. Based on Handschuh et al. [32], X-ray tubes with 40 and 80 kVp voltages were selected for DECT imaging. The X-ray energy spectrum, generated by Spekpy simulation [33], is shown in Fig. 2. XACT and XPCT used a 40 kVp X-ray source, whereas DECT used 40 and 80 kVp sources. Glass filter (1.1 mm) and aluminum filter (0.5 mm) were placed before the 40 and 80 kVp tubes to reduce beam-line hardening. Source and detector pixels were 40 and 62 μm, respectively, with the detector having 200 single-row pixels. The system's magnification factor was 1.25, yielding a reconstructed voxel size of 49.6 μm. Projection data were acquired at 1-degree intervals, obtaining 360 images per

**Table 1** The relevant parameters of the system setups depicted in Fig. 1

| X-ray energy (LE) | X-ray energy (HE) | X-ray focus size | $Z_{sd}$ | M (Magnification) | Projections per rotation | Number of photons physically emitted per projection |
|---|---|---|---|---|---|---|
| 40 kVp | 80 kVp | 40 μm | 100 cm | 1.25 | 360 | $4 \times 10^7$ |
| Projection mask aperture | Projection mask period | Pixels number | Pixel | Voxel | Mask material | Mask thickness |
| 12.4 μm | 124 μm | 1×200 | 62 μm | 49.6 μm | Gold | 80 μm |

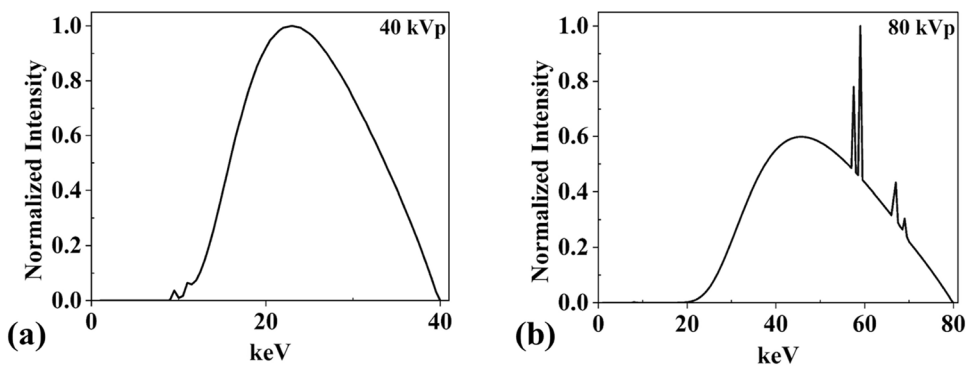


**Fig. 2** The emission spectra of X-ray sources. **a** is the emission spectrum at a tube voltage of 40 kVp, and **b** is the emission spectrum at a tube voltage of 80 kVp (high energy for DECT only)

**Table 2** Soft-tissue phantom component elements. The unit of material density is g/cm$^3$. All values of the elemental composition are in %

| Position | Plug | Material density | Elemental composition | | | | | | | | | |
|---|---|---|---|---|---|---|---|---|---|---|---|---|
| | | | H | C | N | O | Na | P | S | Cl | K | Ca |
| Right | Lung (inhale) | 0.20 | 8.8 | 67.5 | 3.5 | 18.6 | – | – | – | 1.6 | – | – |
| Left | Lung (exhale) | 0.50 | 9.8 | 70.2 | 2.3 | 15.1 | – | – | – | 1.0 | – | 1.6 |
| Top | Adipose | 0.96 | 9.4 | 72.4 | 2.3 | 15.5 | – | – | – | 0.2 | – | 0.3 |
| Bottom | Water (liquid) | 1.00 | 66.0 | – | – | 34.0 | – | – | – | – | – | – |
| Background | Soft tissue | 1.03 | 10.5 | 25.6 | 2.7 | 60.2 | 0.1 | 0.2 | 0.3 | 0.2 | 0.2 | – |

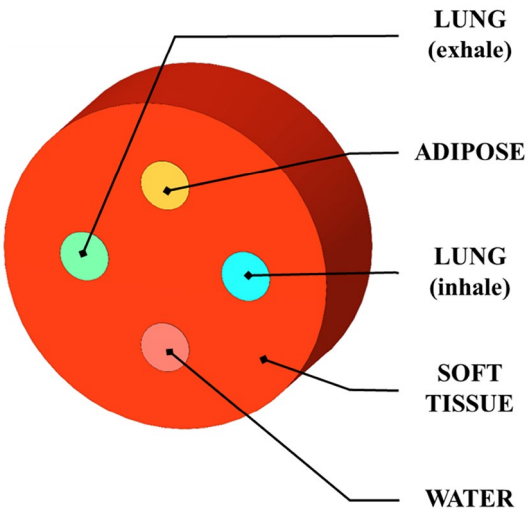


**Fig. 3** (Color online) Schematic view of the soft-tissue phantom model. The soft-tissue phantom consists of nested tubes with soft tissue as the base, with four component material plugs positioned at four locations. The radius of the disk is 4 mm, while the radius of the plugs is 0.6 mm. The height of the phantom is 2 mm

rotation. XACT emitted $4 \times 10^7$ photons per angle, whereas DECT emitted $2 \times 10^7$ photons due to dual voltage requirements. In XPCT, the $y$-direction resolution was halved per Eq. 5; however, linear interpolation achieved 49.6 µm voxel size for comparison. The mask's projected size doubled the pixel size, with beamlets hitting the pixel midpoints. The mask thickness ensured that the X-rays passed only through the apertures, enabling the absorption of almost all 40 kVp X-rays elsewhere. XPCT photon count was increased tenfold to offset the 90% mask loss (i.e., $4 \times 10^8$).

The simulated soft-tissue phantom is shown in Fig. 3, and the corresponding tissue material information is presented in Table 2. The radius of the phantom was 4 mm, whereas those of the other plugs were 0.6 mm. The phantom height was 2 mm. Tissue material data were obtained from CIRS 062 M phantom and International Commission on Radiological Protection. The $\mu(E)$ of the phantom was obtained from the database of the National Institute of Standards and Technology and $\delta$ was calculated as $\delta = 4.15 \times 10^{-4} \rho Z/(AE^2)$ [27].

The system setup in GEANT4 corresponds to that shown in Fig. 1. The GEANT4 simulation program for SMSS EI-based XPCT is optimized by Brombal et al. [34, 35]. The energy spectrum is input into the source module, generating photons with the same distribution as in Fig. 2. In the SMSS EI system, photons must pass through the mask and hit the center of two pixels precisely, making mask position calibration essential. The mask must meet requirements in both $y$ and $z$ directions. For $y$-direction calibration, the normalized intensity position of 0.5 is determined by extracting the single-mask IC curve [36], as shown in Fig. 4a, ensuring the photon reaches the detection unit's middle position. For $z$-direction calibration, the mask is moved until achieving a uniform image. The refractive angle signal at this $z$-position, shown in Fig. 4b, confirms $z$-direction requirements are met. Table 2 and $\delta$ containing phantom information are input into

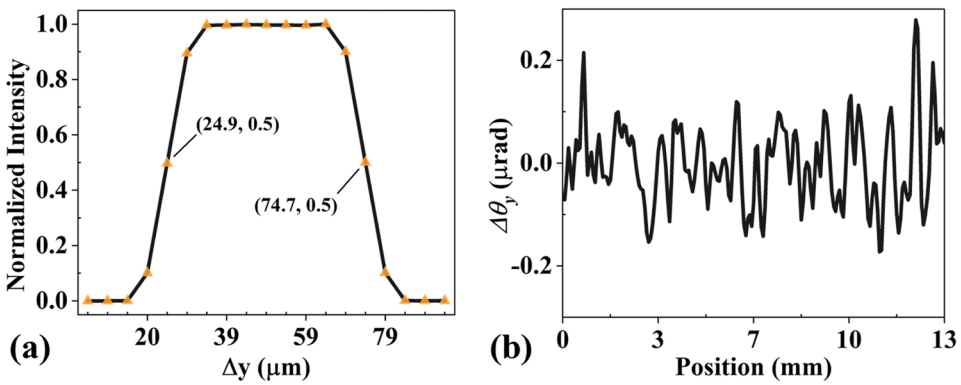


**Fig. 4** (Color online) **a** IC curve for single-mask, **b** is the refractive angle signal extracted by the XPCT after the mask position is well calibrated

the object module. The soft-tissue phantom has five solid parts. We add an object rotation module to adjust positions and rotations during scanning, as the original program lacks direct phantom rotation. Using Python scripting, the program enables simultaneous multitasking and multithreading for efficient simulation.

The data read by the detector are imported into MATLAB for processing and imaging, as shown in Fig. 5. Projection images are presented by moving the object in the $x$-direction to show the projected image with a larger field of view, with CT imaging only imaging a certain height. The simulated profiles in Fig. 5b, g, h and q closely match theoretical profiles. For XACT imaging, 360-degree projections are acquired, and the projection sinogram is obtained using the *fanbeam* function, followed by *ifanbeam* for the sliced image. Hamming filters are used in all back-projection (BP) procedures except Fig. 5w. The XACT image contrast in Fig. 5d originates from linear absorption coefficient $\mu$. DECT imaging is based on

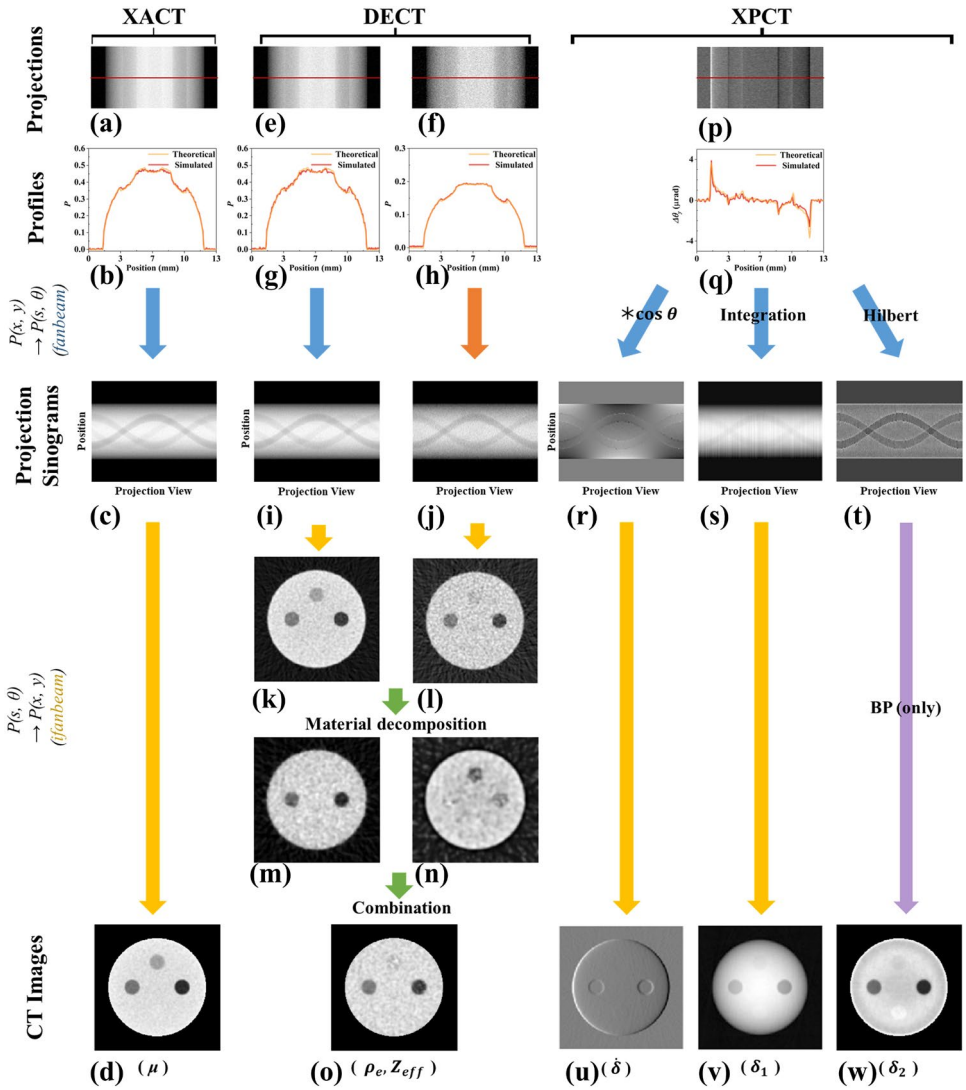


**Fig. 5** (Color online) Schematic of imaging data processing for XACT, DECT, and XPCT with MATLAB. **a**, **e**, **f**, and **p** are the raw projections obtained by GEANT4. **b**, **g**, **h**, and **h** show the red profiles corresponding to the projections and the theoretically calculated curves in orange. **c**, **i**, **j**, **r**, **s**, and **t** are projection sinograms. **d**, **k**, **l**, **u**, **v**, and **w** are the sliced images obtained after the *ifanbeam* operation. Note that the Hamming window filtering is added to all except **w** which is an only BP operation. **m** and **n** are the relative electron density $\rho_e$ image and the effective atomic number $Z_{eff}$ image of **k** and **l** decomposed with calcium and water as the base material, respectively, which can be combined together to obtain the DECT image **o** with $\rho_e$ and $Z_{eff}$ as the contrast. The blue and orange arrows show the operation of *fanbeam* after acquiring multiple projected profiles at low and high energies, respectively. The yellow arrows indicate the operation of FBP after obtaining the projection sinograms. The green arrow indicates a processing operation for dual-energy operation, which recombines the low-energy and high-energy images after material decomposition. The purple arrow indicates the operation of BP only after obtaining the projection sinograms

XACT, with material decomposition performed on low-energy (Fig. 5k) and high-energy (Fig. 5l) images. Figure 5k appears sharper due to decreased X-ray interaction cross-section at higher energies. Using calcium and water as basis materials ($\mu$ values: (calcium) 8.31 and 1.47 $cm^{-1}$; (water) 0.69 and 0.25 $cm^{-1}$ at 40 and 80 kVp, respectively), Eqs. 2, 3, and 4 yield relative electron density $Z_{eff}$ and effective atomic number images in Fig. 5m and n. The DECT image contrast in Fig. 5o combines normalized $Z_{eff}$ values. XPCT imaging requires complex *fanbeam* transformation due to non-constant $\triangle\theta_y$. Three solutions—cos $\theta$ multiplication, direct integration, and Hilbert transform—yield projection sinograms (Fig. 5r, s and t), with resulting slice images (Fig. 5u, v, and w). Figure 5t shows center brightness due to direct integration effects. XPCT images u, v, and w contrast originates from differential phase $\dot{\delta}$, phase $\delta_1$, and phase $\delta_2$. Detailed algorithms are reported in reference [31, 35, 37].

For a better comparison with the simulation results, we additionally built theoretical CT images of XACT, DECT, and XPCT of the phantom with the same voxel based on MATLAB. After modeling in MATLAB, the same process was performed, as shown in Fig. 5. The next step involves the development of methods to evaluate these results.

### 2.3 Evaluation system

In this study, the performance of DECT, XPCT, and XACT was assessed through a comprehensive evaluation system based on four aspects: error evaluation metrics, image quality evaluation metrics, contrast and noise evaluation metrics, and data distribution and dispersion evaluation metrics. The error evaluation metrics include the absolute error (AE) and mean absolute error (MAE), which are calculated using Eqs. 7 and 8, respectively, to assess the difference between the measured and theoretical values for different tissues. The image quality evaluation metrics consist of the structural similarity index (SSIM) and peak signal-to-noise ratio (PSNR), where the former compares the similarity between two images, and the latter measures the noise level and distortion of the image, as indicated by Eqs. 9 and 10. The contrast and noise evaluation metrics, represented by the contrast-to-noise ratio (CNR) defined in Eq. 11, assess the clarity and noise level of the reconstructed images. The data distribution and dispersion evaluation metrics were represented by boxplots that visually displayed the distribution and dispersion of the data, including the minimum, lower, median, upper, and maximum values. This method helps visualize the distribution and dispersion of the measurement data, aiding in the identification of outliers and the shape of the data distribution.

$$\mathrm{AE} = \left| O_{\mathrm{measured}} - O_{\mathrm{theoretical}} \right| \tag{7}$$

$$\mathrm{MAE} = \frac{1}{n} \sum_{i=0}^{n} \left| O^{i}_{\mathrm{measured}} - O^{i}_{\mathrm{theoretical}} \right| \tag{8}$$

$$\mathrm{SSIM} = \frac{2A_{\mathrm{measured}}A_{\mathrm{theoretical}} + C_1}{A^2_{\mathrm{measured}} + A^2_{\mathrm{theoretical}} + C_1} \cdot \frac{2\sigma_{\mathrm{measured,theoretical}} + C_2}{\sigma^2_{\mathrm{measured}} + \sigma^2_{\mathrm{theoretical}} + C_2} \tag{9}$$

$$\mathrm{PSNR} = 10 \times \log_{10} \left( \frac{\mathrm{Peakval}^2}{\mathrm{MSE}} \right) \tag{10}$$

$$\mathrm{CNR} = \frac{\left| O_{\mathrm{signal}} - O_{\mathrm{background}} \right|}{\sqrt{\sigma^2_{\mathrm{signal}} + \sigma^2_{\mathrm{background}}}} \tag{11}$$

In Eqs. 7 and 8, $O$ denotes the observed value, where $i$ represents the voxel point, and $n$ is the total voxel count of different tissues. In Eq. 9, $A_{\mathrm{measured}}$, $A_{\mathrm{theoretical}}$, $\sigma^2_{\mathrm{measured}}$, $\sigma^2_{\mathrm{theoretical}}$, and $\sigma_{\mathrm{measured,theoretical}}$ are the local mean, variance, and covariance of the measured and theoretical images, respectively, and $C_1$ and $C_2$ are stability constants. In Eq. 10, Peakval represents the maximum observed value in an image. MSE is the mean squared error between the measured and theoretical images. In Eq. 10, $O_{\mathrm{signal}}$ and $O_{\mathrm{background}}$ represent the intensities of the signal and background, respectively, and $\sigma^2$ is the corresponding variance.

## 3 Results and discussion

### 3.1 CT images

Following the reconstruction algorithms described in Sect. 2.2, we obtained slice images for the three techniques as shown in Fig. 6. All the images share identical ROIs, with normalized image intensities. To reveal hidden textures, we use pseudo-color representation, mapping grayscale values to the RGB color range. The colorbar indicates normalized intensity. The lung (inhale) region appears blue, lung (exhale) appears green, adipose appears orange, and water and soft-tissue regions appear in varying shades of red. The similar colors for water and soft tissue reflect their comparable densities. In subsequent analyses, the distinction between water and soft tissue serves as a reference for imaging technology resolution—clearer distinction indicates better discriminatory ability. From the theoretical images in Fig. 6a and c, XACT and DECT show similar image contrasts due to their shared principle of intensity attenuation. While the performance of XPCT differs from that of absorption imaging

techniques, advantages and disadvantages cannot be determined through simple observations.

For simulated images, XACT and DECT show similar characteristics, both struggling with water detection, with DECT showing higher noise due to emitting half the photons as XACT in two emissions. In XPCT, we selected Fig. 5w for comparison. The XPCT noise differs from Gaussian noise in absorption images, showing slight ringing artifacts [38], but edges remain clearly visible in all five materials.

For quantitative analysis, we extracted information from each image, as shown by white boxes in Fig. 6a, with results depicted in Fig. 7. Panels a, b, and c in Fig. 7 show the intensity profiles of XACT, DECT, and XPCT images, respectively, against soft-tissue background. XPCT demonstrates the best profile smoothing and shows water's signal intensity, which is not reflected by absorption-contrast imaging. The statistical evaluation process is detailed in the next section.

## 3.2 Statistical evaluation

The physical quantities reconstructed from the simulated images and the AE results are compared with the theoretical values in Table 3. Among these, DECT exhibited the largest deviation, which was due to the halving of the dose per emission, leading to relatively poor performance in the simulated images. Conversely, XPCT had the smallest AE, indicating a closer alignment with the theoretical values.

Furthermore, we compare the SSIM and PSNR values of the images shown in Fig. 6, and the results are listed in Table 4. These two metrics are calculated using the simulated and theoretical images. Larger SSIM and PSNR values indicate better-simulated images. Evidently, XPCT is the closest to the theoretical image and exhibits the least noise effect. XACT and DECT do not perform well on image quality assessment metrics because of the effect of Gaussian noise.

Table 5 displays the theoretical and simulated CNR results of the images in Fig. 7. The theoretical CNR shows XACT and DECT have similar resolving power. XACT performs better for tissues with large density differences, while DECT excels for tissues with small density differences. XPCT shows the highest CNR for large density differences, with resolving power between DECT and XACT for small density differences. In simulated results, DECT performs the worst overall, while XACT surpasses XPCT for tissues with large density differences, and XPCT excels for similar-density tissues. The theoretical CNR values are on the order of $10^{14}$, approaching infinity; however, reconstruction algorithm noise prevents infinite values. Simulated CNR values are lower due to noise impact. Comparing both on the same scale reveals XACT maintains excellent resolution for high density differences, XPCT performs the best for smaller differences, while DECT shows weakest performance, primarily due to photon statistical fluctuations proportional to the square root of emitted particles. In the DECT simulated results, increased statistical fluctuation from halving the photon emission affects both low-energy and high-energy slice images. Both projections deviate from true values due to statistical fluctuations. When performing material

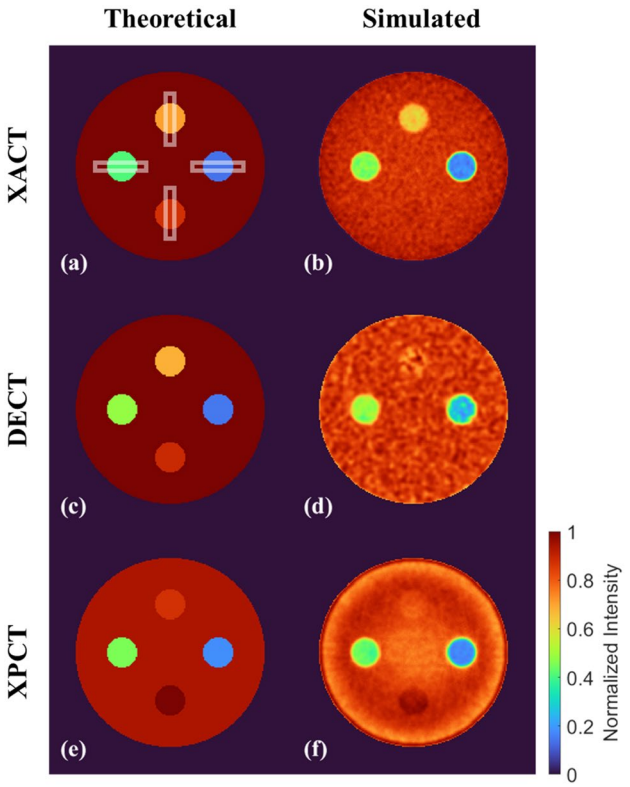


**Fig. 6** (Color online) CT image results. **a**, **c**, and **e** are theoretical images of XACT, DECT, and XPCT, respectively. **b**, **d**, and **f** are simulated images of XACT, DECT, and XPCT, respectively

**Table 3** Simulation results and AE results compared with theoretical values

| | | Lung (inhale) | Lung (exhale) | Adipose | Water (liquid) | Soft-tissue (background) |
|---|---|---|---|---|---|---|
| XACT | $\mu$ ($cm^{-1}$) | 0.12 ± 8.03% | 0.35 ± 7.30% | 0.49 ± 11.21% | 0.71 ± 4.33% | 0.69 ± 1.51% |
| DECT | $\rho_e$ ($\times 10^{22}$ $cm^{-3}$) | 0.65 ± 3.26% | 1.58 ± 5.82% | 3.29 ± 10.55% | 2.97 ± 11.33% | 3.27 ± 6.03% |
| | $Z_{eff}$ | 7.89 ± 1.33% | 10.76 ± 17.49% | 7.31 ± 14.55% | 11.41 ± 14.09% | 10.58 ± 11.58% |
| XPCT | $\delta$ ($\times 10^{-8}$) | 2.09 ± 1.32% | 5.12 ± 0.56% | 9.89 ± 0.35% | 11.44 ± 0.50% | 10.61 ± 0.17% |

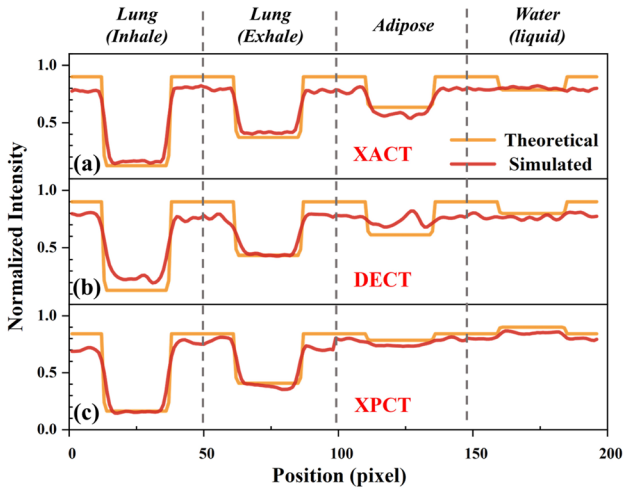


**Fig. 7** (Color online) Profiles of the CT images in Fig. 6. Panels **a**, **b** and **c** represent profiles of the XACT, DECT, and XPCT images, respectively. The orange lines are from theoretical images, and the red lines are from simulated images

**Table 4** SSIM and PSNR results for the simulated and theoretical images in Fig. 6 and MAE results for the images in Fig. 7

| | SSIM | PSNR | MAE |
|---|---|---|---|
| XACT | 0.87 | 21.17 | 0.083 |
| DECT | 0.81 | 19.68 | 0.106 |
| XPCT | 0.89 | 21.47 | 0.061 |

**Table 5** Theoretical and simulated CNR results for XACT, DECT, and XPCT calculated from Fig. 7

| | | Lung (inhale) | Lung (exhale) | Adipose | Water (liquid) |
|---|---|---|---|---|---|
| XACT | Theoretical ($\times 10^{14}$) | 23.10 | 15.52 | 7.47 | 2.36 |
| | Simulated | 36.60 | 22.61 | 10.07 | 1.05 |
| DECT | Theoretical ($\times 10^{14}$) | 22.88 | 12.33 | 8.10 | 3.03 |
| | Simulated | 17.05 | 16.34 | 0.83 | 0.57 |
| XPCT | Theoretical ($\times 10^{14}$) | 30.11 | 18.78 | 2.54 | 2.57 |
| | Simulated | 14.63 | 8.68 | 1.26 | 3.92 |

decomposition using Eq. 2, this deviation amplifies errors in calculating $b_1$ and $b_2$ [39]. Boxplots from Fig. 6 are shown in Fig. 8. White lines indicate median position, while white dots show mean position. Box height shows data dispersion, with bottom and top edges at 25th and 75th percentiles. The whiskers extend to the remaining data range. The boxplots show that XPCT has better data distribution than do DECT and XACT, indicating better phase information reconstruction and extraction.

In brief, this section provides a quantitative evaluation of DECT and XPCT compared to XACT. Results show XPCT performs relatively better in several performance metrics.

While the SMSS EI-based XPCT method is easier to implement, misalignments in mask position during gantry movement can invalidate calibration, requiring more precise equipment. Radiation safety is crucial in medical applications. Though radiation dose is comparable, exposure time is significantly longer due to reduced X-ray efficiency. Research shows optimizing the mask [40] and reducing exposure through low-dose irradiation [31] can address this. The method requires specific detector capabilities, as pixel crosstalk affects detection sensitivity, making direct-conversion or photon-counting detectors more suitable.

In this study, soft-tissue models with low-density and similar tissues are used owing to limited data on other tissues, and such tissue differentiation remains challenging in clinical diagnosis. XPCT offers a new technique for this, though complex situations require further biological experiments for resolution.

## 4 Conclusion

In this study, we performed a systematic comparative evaluation of DECT and SMSS EI-based XPCT for soft-tissue phantoms using a comprehensive evaluation system. Multiple metrics demonstrate that XPCT outperformed DECT, due to XPCT's sensitivity to low-density objects and excessive statistical fluctuations in DECT. The SMSS EI-based XPCT shows potential for fast, accurate

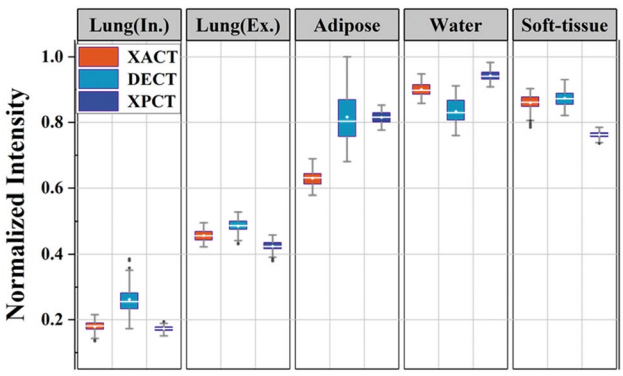


**Fig. 8** (Color online) Boxplots calculated from CT simulated results in Fig. 6

imaging through its simple, robust setup. This system provides a reliable method for evaluating imaging technology advancements and comparing algorithms, enabling efficient quantitative analysis for non-specialists. These findings confirm XPCT's significance in medical research and its sensitivity to low-density objects.

For objects with similar densities, XPCT shows clear advantages, whereas XACT excels with small densities and large differences, and DECT has optimization potential in algorithms and absorbed dose. In XPCT, SMSS EI method optimally balances device complexity and phase information extraction accuracy. The SMSS EI method's noise resistance and simple setup enable practical low-dose, large field XPCT applications. The widespread adoption of XPCI technology in medical fields like lung, breast, musculoskeletal, and dental imaging is inevitable [41]. Challenges remain in radiation dose, acquisition time, field restrictions, and stability. Due to dose limitations, DECT requires more focus on dose restrictions, making radiation dose reduction a key research area, with dual-layer or photon-counting detectors showing promise [42–45]. XPCI development will advance through sources, absorption masks, phase gratings, and detectors, with hardware and hybrid upgrades impacting XPCT information extraction [46].

**Author Contributions** All authors contributed to the study conception and design. Material preparation, data collection, and analysis were performed by Chang Li, Xiao-Xuan Ren, and Liang-Liang Lv. The first draft of the manuscript was written by Chang Li and all authors commented on previous versions of the manuscript. All authors read and approved the final manuscript.

**Data Availability** The data that support the findings of this study are openly available in Science Data Bank at https://cstr.cn/31253.11.sciencedb.j00186.00940 and https://doi.org/10.57760/sciencedb.j00186.00940.

## Declarations

**Conflict of interest** The authors declare that they have no conflict of interest.

## References


1. X. Ou, X. Chen, X. Xu et al., Recent development in X-ray imaging technology: future and challenges. Research **2021**, 9892152 (2021). https://doi.org/10.34133/2021/9892152
2. S. Tao, C. He, X. Hao et al., Principles of different X-ray phase-contrast imaging: a review. Appl. Sci. **11**, 2971 (2021). https://doi.org/10.3390/app11072971
3. M. Endrizzi, X-ray phase-contrast imaging. Nucl. Instrum. Meth. A **878**, 88–98 (2018). https://doi.org/10.1016/j.nima.2017.07.036
4. X. Zhang, T. Su, J. Yang et al., Performance evaluation of dual-energy CT and differential phase contrast CT in quantitative imaging applications. Med. Phys. **49**, 1123–1138 (2022). https://doi.org/10.1002/mp.15417
5. X. Xia, X. Hu, J. Zou, Dual-energy X-ray computed tomography study based on CsI: Tl and LYSO: Ce scintillator combination. J. Appl. Phys. **130**, 234902 (2021). https://doi.org/10.1063/5.0066085
6. A. Momose, Demonstration of phase-contrast X-ray computed tomography using an X-ray interferometer. Nucl. Instrum. Meth. A **352**, 622–628 (1995). https://doi.org/10.1016/0168-9002(95)90017-9
7. L. Brombal, G. Kallon, J. Jiang et al., Monochromatic propagation-based phase-contrast microscale computed-tomography system with a rotating-anode source. Phys. Rev. Appl. **11**, 034004 (2019). https://doi.org/10.1103/PhysRevApplied.11.034004
8. I. Häggmark, K. Shaker, S. Nyrén et al., Phase-contrast virtual chest radiography. Proc. Natl. Acad. Sci. USA **120**, e2210214120 (2023). https://doi.org/10.1073/pnas.2210214120
9. Y. Li, Y. Zhao, D. Ji et al., Sparse-domain regularized stripe decomposition combined with guided-image filtering for ring artifact removal in propagation-based X-ray phase-contrast CT. Phys. Med. Biol. **66**, 105011 (2021). https://doi.org/10.1088/1361-6560/abf9de
10. H. Wang, Y. Kashyap, K. Sawhney, Quantitative X-ray dark-field and phase tomography using single directional speckle scanning technique. Appl. Phys. Lett. **108**, 124102 (2016). https://doi.org/10.1063/1.4944462
11. M.K. Croughan, Y.Y. How, A. Pennings et al., Directional dark-field retrieval with single-grid X-ray imaging. Opt. Express **31**, 11578 (2023). https://doi.org/10.1364/OE.480031
12. T.J. Davis, D. Gao, T.E. Gureyev et al., Phase-contrast imaging of weakly absorbing materials using hard X-rays. Nature **373**, 595–598 (1995). https://doi.org/10.1038/373595a0
13. Y.B. Wang, G.P. Li, X.D. Pan et al., An improved multiple-image radiography method extracting refraction information in analyzer-based imaging. Nucl. Instrum. Meth. A **770**, 182–188 (2015). https://doi.org/10.1016/j.nima.2014.10.035
14. R. Tang, Y. Li, L. Qin et al., Phase retrieval-based phase-contrast CT for vascular imaging with microbubble contrast agent. Med. Phys. **48**, 3459–3469 (2021). https://doi.org/10.1002/mp.14819
15. F. Pfeiffer, M. Bech, O. Bunk et al., Hard-X-ray dark-field imaging using a grating interferometer. Nat. Mater. **7**, 134–137 (2008). https://doi.org/10.1038/nmat2096
16. Z.F. Huang, K.J. Kang, L. Zhang et al., Alternative method for differential phase-contrast imaging with weakly coherent hard X-rays. Phys. Rev. A **79**, 013815 (2009). https://doi.org/10.1103/PhysRevA.79.013815
17. J. Yang, J.H. Huang, Y.H. Lei et al., Analysis of period and visibility of dual phase grating interferometer. Chin. Phys. B **31**, 058701 (2022). https://doi.org/10.1088/1674-1056/ac3a60
18. C.X. Wei, Z. Wu, F. Wali et al., Single-shot grating-based X-ray differential phase contrast imaging with a modified analyzer grating. Chin. Phys. B **26**, 108701 (2017). https://doi.org/10.1088/1674-1056/26/10/108701
19. Z. Wu, W.B. Wei, K. Gao et al., Prototype system of noninterferometric phase-contrast computed tomography utilizing medical imaging components. J. Appl. Phys. **129**, 074901 (2021). https://doi.org/10.1063/5.0031392
20. W. Tao, Y. Sung, S.J.W. Kim et al., Tomography of dark-field scatter including single-exposure Moiré fringe analysis with X-ray biprism interferometry–A simulation study. Med. Phys. **48**, 6293–6311 (2021). https://doi.org/10.1002/mp.15134
21. A. Olivo, R. Speller, A coded-aperture technique allowing X-ray phase contrast imaging with conventional sources. Appl. Phys. Lett. **91**, 074106 (2007). https://doi.org/10.1063/1.2772193
22. A. Olivo, S. Gkoumas, M. Endrizzi et al., Low-dose phase contrast mammography with conventional X-ray sources. Med. Phys. **40**, 090701 (2013). https://doi.org/10.1118/1.4817480

23. L. Massimi, S.J. Clark, S. Marussi et al., Dynamic multicontrast X-ray imaging method applied to additive manufacturing. Phys. Rev. Lett. **127**, 215503 (2021). https://doi.org/10.1103/PhysRevLett.127.215503
24. L. Heck, J. Herzen, Recent advances in X-ray imaging of breast tissue: from two- to three-dimensional imaging. Phys. Med. **79**, 69–79 (2020). https://doi.org/10.1016/j.ejmp.2020.10.025
25. M. Viermetz, N. Gustschin, C. Schmid et al., Dark-field computed tomography reaches the human scale. Proc. Natl. Acad. Sci. USA **119**, e2118799119 (2022). https://doi.org/10.1073/pnas.2118799119
26. P.R.T. Munro, K. Ignatyev, R.D. Speller et al., Phase and absorption retrieval using incoherent X-ray sources. Proc. Natl. Acad. Sci. USA **109**, 13922–13927 (2012). https://doi.org/10.1073/pnas.1205396109
27. C. Zhang, X. Pan, H. Shang et al., Evaluating the effects of source conditions on coded-aperture based X-ray phase contrast imaging. Eur. Phys. J. Appl. Phys. **83**, 10701 (2018). https://doi.org/10.1051/epjap/2018180040
28. F. Krejci, J. Jakubek, M. Kroupa, Single grating method for low dose 1-D and 2-D phase contrast X-ray imaging. J. Instrum. **6**, C01073 (2011). https://doi.org/10.1088/1748-0221/6/01/C01073
29. P.P. Zhu, J.Y. Wang, Q.X. Yuan et al., Computed tomography algorithm based on diffraction-enhanced imaging setup. Appl. Phys. Lett. **87**, 264101 (2005). https://doi.org/10.1063/1.2155117
30. J. Wang, P. Zhu, Q. Yuan et al., Reconstruction of the refractive index gradient by X-ray diffraction enhanced computed tomography. Phys. Med. Biol. **51**, 3391–3396 (2006). https://doi.org/10.1088/0031-9155/51/14/007
31. C. Zhang, C. Li, J. Qi et al., Simulations of single-shot X-ray phase-contrast tomography based on edge illumination. Nucl. Instrum. Meth. A **983**, 164598 (2020). https://doi.org/10.1016/j.nima.2020.164598
32. S. Handschuh, C.J. Beisser, B. Ruthensteiner et al., Microscopic dual-energy CT (microDECT): a flexible tool for multichannel ex vivo 3D imaging of biological specimens. J. Microsc. **267**, 3–26 (2017). https://doi.org/10.1111/jmi.12543
33. G. Poludniowski, A. Omar, R. Bujila et al., Technical note: SpekPy v2.0–a software toolkit for modeling X-ray tube spectra. Med. Phys. **48**, 3630–3637 (2021). https://doi.org/10.1002/mp.14945
34. L. Brombal, L. Rigon, F. Arfelli et al., A Geant4 tool for edge-illumination X-ray phase-contrast imaging. J. Inst. **17**, C01043 (2022). https://doi.org/10.1088/1748-0221/17/01/C01043
35. L. Brombal, F. Arfelli, R.H. Menk et al., PEPI Lab: a flexible compact multi-modal setup for X-ray phase-contrast and spectral imaging. Sci. Rep. **13**, 4206 (2023). https://doi.org/10.1038/s41598-023-30316-5
36. G.K. Kallon, P.C. Diemoz, F.A. Vittoria et al., Comparing signal intensity and refraction sensitivity of double and single mask edge illumination lab-based X-ray phase contrast imaging set-ups. J. Phys. D Appl. Phys. **50**, 415401 (2017). https://doi.org/10.1088/1361-6463/aa8692
37. N. Francken, J. Sanctorum, P. Paramonov et al., Edge illumination X-ray phase contrast simulations using the CAD-ASTRA toolbox. Opt. Express **32**, 10005 (2024). https://doi.org/10.1364/OE.516138
38. B. Yu, G. Li, J. Zhang et al., Enhancing contrast of spatial details in X-ray phase-contrast imaging through modified Fourier filtering. Photonics **10**, 1204 (2023). https://doi.org/10.3390/photonics10111204
39. Y. Yao, L. Li, Z. Chen, Iterative dynamic dual-energy CT algorithm in reducing statistical noise in multi-energy CT imaging. Phys. Med. Biol. **67**, 015003 (2022). https://doi.org/10.1088/1361-6560/ac459d
40. P.J. Vanthienen, J. Sanctorum, B. Huyge et al., Alternative grating designs for cone-beam edge illumination X-ray phase contrast imaging, in *Developments in X-ray tomography XIV*, vol. 34, ed. by B. Müller, G. Wang (SPIE, Bellingham, 2022). https://doi.org/10.1117/12.2632301
41. F. Pfeiffer, J. Herzen, M. Willner et al., Grating-based X-ray phase contrast for biomedical imaging applications. Z. Med. Phys. **23**, 176–185 (2013). https://doi.org/10.1016/j.zemedi.2013.02.002
42. D. Odedra, S. Narayanasamy, S. Sabongui et al., Dual energy CT physics–a primer for the emergency radiologist. Front. Radio **2**, 820430 (2022). https://doi.org/10.3389/fradi.2022.820430
43. Y. Liu, C. Gao, D. Li et al., Dynamic X-ray imaging with screen-printed perovskite CMOS array. Nat. Commun. **15**, 1588 (2024). https://doi.org/10.1038/s41467-024-45871-2
44. H. Chen, Y. Fang, J. Gu et al., Dual-layer spectral detector computed tomography quantitative parameters: a potential tool for lymph node activity determination in lymphoma patients. Diagnostics **14**, 149 (2024). https://doi.org/10.3390/diagnostics14020149
45. W.B. Ma, C.F. Kuang, X. Liu et al., Research progress of X-ray detection and imaging based on emerging metal halide semiconductors and scintillators. Acta Opt. Sin. **42**, 1704002 (2022). https://doi.org/10.3788/AOS202442.1704002
46. L. Yi, B. Hou, H. Zhao et al., X-ray-to-visible light-field detection through pixelated colour conversion. Nature **618**, 281–286 (2023). https://doi.org/10.1038/s41586-023-05978-w